Dalton Transactions

ROYAL SOCIETY OF CHEMISTRY

PAPER

View Article Online
View Journal | View Issue

Check for updates

Cite this: *Dalton Trans.*, 2023, **52**, 6484

Enantiopure cycloplatinated pentahelicenic N-heterocyclic carbenic complexes that display long-lived circularly polarized phosphorescence†

Debsouri Kundu,[a] Natalia del Rio,[a] Marie Cordier,[a] Nicolas Vanthuyne,[b] Emma V. Puttock,[c] Stefan C. J. Meskers,[d] J. A. Gareth Williams,*[c] Monika Srebro-Hooper*[e] and Jeanne Crassous*[a]

Received 23rd February 2023,
Accepted 16th April 2023

DOI: 10.1039/d3dt00577a

rsc.li/dalton

The preparation of the first enantiopure cycloplatinated complexes bearing a bidentate, helicenic N-heterocyclic carbene and a diketonate ancillary ligand is presented, along with their structural and spectroscopic characterization based on both experimental and computational studies. The systems exhibit long-lived circularly polarized phosphorescence in solution and in doped films at room temperature, and also in a frozen glass at 77 K, with dissymmetry factor g_{lum} values $\geq 10^{-3}$ in the former and around 10^{-2} in the latter.

Introduction

N-heterocyclic carbenes (NHCs) have become classical ligands for organometallic and coordination chemistry[1] thanks to their strong σ-donor abilities that result in the formation of stable metal–carbon bonds. The introduction of chirality in NHC-based complexes has opened up a variety of applications for such molecules, for example in enantioselective catalysis[2] and chiral materials science.[3] Meanwhile, there has been intensive research into phosphorescent complexes of heavy metals,[4,5] such as iridium(III) and platinum(II), including systems with NHC ligands, due to their importance as triplet-harvesting phosphors in organic light-emitting diodes (OLEDs).[6,7]

The design of chiral emitters displaying intense circularly polarized luminescence (CPL) has attracted significant interest, thanks to the potential of circularly polarized (CP) light in a diverse range of applications from OLEDs and optical information processing to bio-imaging and chiral sensing.[8] For example, CP-OLEDs offer an interesting approach to improve the performance of high-resolution displays by eliminating the need for anti-glare polarized filters, which can account for the loss of up to 50% of the emitted light.[9] Although many types of chiral NHC-complexes with diverse stereogenic elements have been developed to date, especially for enantioselective catalysis, there are very few examples of enantiopure chiroptical materials based on NHC-Pt complexes, and they are mainly limited to those bearing monodentate NHCs.[10]

Our group has developed chiral versions of several classes of organometallic compounds,[11] including complexes incorporating helical NHCs,[12] with intriguing emission properties such as long-lived CP phosphorescence. Inspired by the work of Strassner and co-workers on phosphorescent Pt(II) complexes with (:C^C)-cyclometalating NHC ligands,[7b,13] we tackled the synthesis of their helical analogues. As a result, we describe here the preparation and characterization of the first-of-their-kind enantiopure helicenic NHC-based Pt(II) complexes (see Scheme 1) displaying long-lived CP phosphorescence in solution (both at room and low temperatures) and in thin films (at room temperature). Enantiopure complexes of the form Pt(O^O)(:C^C) have been synthesized, where (:C^C) is an NHC ligand incorporating a [5]helicene unit, and (O^O) is a β-diketonate ligand, *i.e.* either acetylacetonate, acac (**Pt1**) or dibenzoylmethane anion, dbm (**Pt2**). The photophysical (absorption and emission) and chiroptical properties (optical rotation – OR, electronic circular dichroism – ECD, and CPL) of **Pt1** and **Pt2** have been studied both experimentally and computationally.

Results and discussion

Synthesis and structural studies

Following the strategy previously developed in our group to prepare helical NHC ligands,[12] the starting imidazole-fused pentahelicene **1** was subjected to *N*-arylation with 4-iodoani-

[a]*Université de Rennes, CNRS, ISCR – UMR 6226, 35000 Rennes, France. E-mail: jeanne.crassous@univ-rennes1.fr*
[b]*Aix Marseille University, CNRS Centrale Marseille, iSm2, 13284 Marseille, France*
[c]*Department of Chemistry, Durham University, Durham DH1 3LE, UK. E-mail: j.a.g.williams@durham.ac.uk*
[d]*Molecular Materials and Nanosystems and Institute for Complex Molecular Systems, Technische Universiteit Eindhoven, NL 5600, The Netherlands*
[e]*Faculty of Chemistry, Jagiellonian University, Gronostajowa 2, 30-387 Krakow, Poland. E-mail: srebro@chemia.uj.edu.pl*

†Electronic supplementary information (ESI) available. CCDC 2207037. For ESI and crystallographic data in CIF or other electronic format see DOI: https://doi.org/10.1039/d3dt00577a

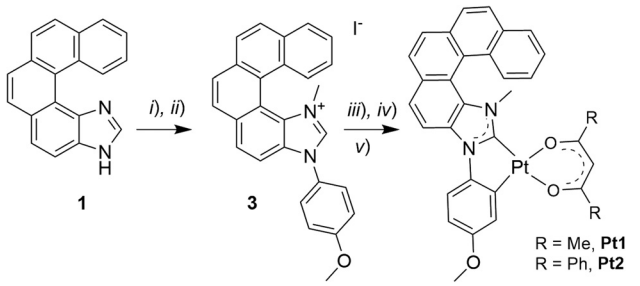

Scheme 1 Synthesis of helicene-NHC-Pt(II) complexes **Pt1** and **Pt2**: (i) 4-iodoanisole, CuI, L-proline, DMSO, 110 °C, 63 h; (ii) CH_3I, CH_3CN, reflux, 16 h (43%, over the 2 steps); (iii) Ag_2O, 1,4-dioxane, rt, 16 h; (iv) *cis*-$Pt(DMSO)_2Cl_2$, toluene, reflux, 16 h; (v) 2,4-pentanedione (acacH) or dibenzoylmethane (dbmH), Na_2CO_3, toluene, reflux, overnight (35% for **Pt1** and 58% for **Pt2**, over the 3 steps).

sole using CuI/L-proline as the catalytic system (Ullman-type coupling), as presented in Scheme 1,[14] to yield 3*N*-(2-anisyl)-[5]helicene-imidazole (**2**). Methylation with MeI in acetonitrile led to the imidazolium iodide salt **3** with an overall yield of 43% over the two steps. Reaction of the salt with silver(I) oxide, followed by transmetalation with *cis*-$Pt(DMSO)_2Cl_2$,[10d] gave the cycloplatinated intermediate, which was treated without further purification with acacH or dbmH and Na_2CO_3 in refluxing toluene, to obtain (*rac*)-**Pt1** or (*rac*)-**Pt2**, respectively, in moderate yields (35% for **Pt1** and 58% for **Pt2** for the three steps).[15] The identity of the final complexes was confirmed by ^1H and ^{13}C NMR spectroscopy and mass spectrometry (see ESI†). For instance, the imidazolium proton in compound **3** resonating at 10.70 ppm is not present in the ^1H NMR spectra of **Pt1** and **Pt2**, while a signal corresponding to the CH proton of the β-diketonate appears at respectively 5.53 and 6.80 ppm in the products.

In addition, suitable crystals of racemic **Pt2** for X-ray diffraction analysis were obtained by slow evaporation of a dichloromethane solution at room temperature (Fig. 1 and ESI†). The resulting (*rac*)-**Pt2**·CH_2Cl_2 crystallized in the $P\bar{1}$ triclinic space group. The d^8 Pt(II) ion adopts a slightly distorted square-planar geometry. The metric data of the Pt(II) coordination sphere (metal–ligand bond lengths and valence angles) are in the range typical for those reported for other (:C^C)Pt(acac) complexes,[7b,13,15] with the NHC and (O^O) ligands situated within the same plane and the coordinated anisole phenyl and NHC rings being almost coplanar (twist angle of 1.58°). The $C_{carbene}$–Pt bond distance of 1.940(3) Å is similar to that in other NHC-platinum compounds previously described.[7b,13,15] The complex assembles into heterochiral dimers organized in a head-to-tail fashion, with π–π interactions between coordinated NHC and anisole phenyl rings of opposite helices (centroid–centroid distance of 3.625 Å); see Fig. 1b and c. The intramolecular Pt–Pt distances of 5.772(2) Å are far longer than in other NHC-Pt(II) derivatives reported in the literature (d(Pt–Pt) = 3.276–3.495 Å),[7b,13,15] evidently showing that Pt–Pt interactions are inhibited by the steric hindrance imposed by the helicene unit. Regarding the helicene moiety, it exhibits a helicity angle (dihedral angle between terminal rings) of 49.3°, which is typical for [5]helicenes and consistent with those measured for similar helicene-NHC ligands.[12] These observations indicate extended π-conjugation across the whole (anisole-NHC-helicene-Pt-β-diketonate) molecular system and efficient electronic interaction between the helicene-NHC ligand and the metal, as also supported by the calculated isosurfaces of the frontier molecular orbitals (*vide infra*, Fig. 2e). Note also that, according to the density functional theory (DFT) computations (see ESI† for a description of computational details used in this study and a full set of calculated results), **Pt2** can be assumed to exist in solution as an equal mixture of practically isoenergetic rotamers of the phenyl groups in the dbm moiety (see Fig. S2.1 in ESI†), near-coplanarity of which ensures effective π-electron conjugation within this ligand.[13b]

Photophysical and chiroptical properties

Both of the racemic complexes, **Pt1** and **Pt2,** were then resolved into their constituent enantiomers using HPLC over a chiral stationary phase, yielding (*P*)-(+) and (*M*)-(−) enantiomers with enantiomeric excess (ee) values between 98 and 99.5% (see ESI†), and their absorption and emission properties were examined.

The UV-vis absorption spectra of **Pt1** and **Pt2** were recorded in toluene at room temperature (10^{-5} M), and they are presented in Fig. 2a; note that all ε and $\Delta\varepsilon$ values in this work are

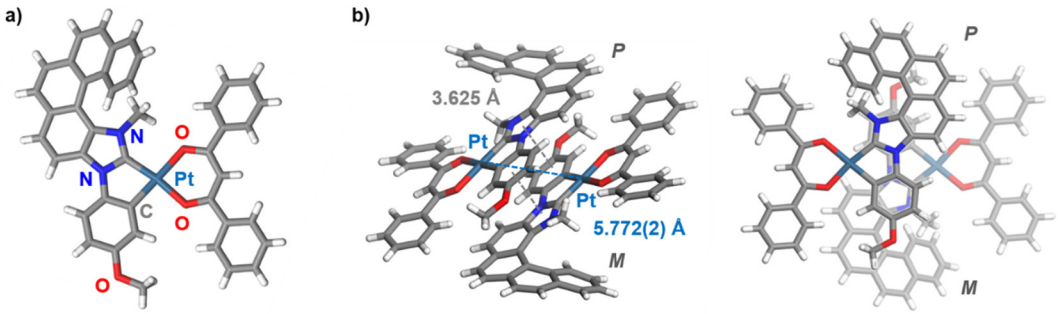

Fig. 1 (a) X-ray crystallographic molecular structure of **Pt2** in (*rac*)-**Pt2**·CH_2Cl_2 along with (b) its supramolecular (head-to-tail) organization into a heterochiral dimer (two views), with π–π interactions and Pt···Pt distances of 3.625 Å and 5.772(2) Å, respectively.

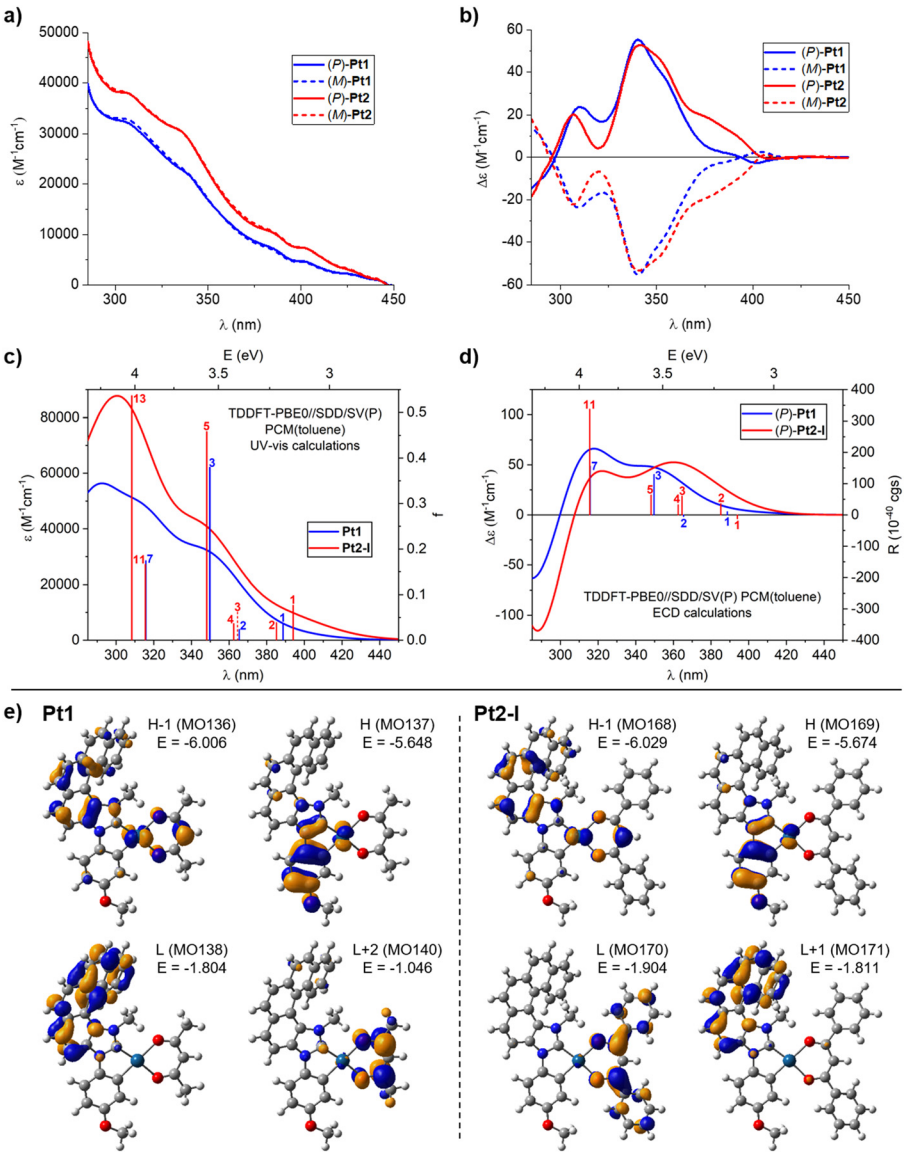

Fig. 2 Experimental (a) UV-visible absorption and (b) ECD spectra of (*P*)-(+) and (*M*)-(–) enantiomers of **Pt1** and **Pt2** measured in toluene at room temperature ($C = 1 \times 10^{-5}$ M) along with the corresponding TDDFT-simulated spectra (panels (c) and (d), respectively; results for the lowest-energy rotamer (l) of **Pt2** shown). (e) Isosurfaces (±0.04 au) of MOs involved in selected electronic transitions of **Pt1** and **Pt2**. See ESI† for a full set of computed data including the electronic assignment of the spectra.

given in units of M^{-1} cm^{-1}. Both complexes exhibit overall very similar spectral envelopes with intense bands at wavelengths shorter than 330 nm, attributable to π–π* transitions within (mainly) the extended π-helical unit (*vide infra*),[11,16] and additional bands of lower intensity at longer wavelengths (ε = 1000–10 000 at λ > 380 nm). It can be seen that the **Pt2** complex exhibits almost uniformly higher UV-vis intensity than **Pt1**.

The ECD spectra of both complexes, **Pt1** and **Pt2**, were also recorded in toluene at room temperature. As depicted in Fig. 2b, the (*P*) and (*M*) enantiomers of each system display the expected mirror-image ECD envelopes. For example, (*P*)-**Pt1** demonstrates two strong positive bands at 309 (+23.9) and 341 (+55.1), accompanied by a positive shoulder at 356 nm (+35.6), and a weak negative band at 401 nm (–2.6). Similarly, (*P*)-**Pt2** shows two strong positive bands at 307 (+20) and 341 (+52.8) with a positive shoulder at 353 nm (+44.4), additional positive bands at 376 (+19) and 390 nm (+11.1), and a very weak negative band at 408 nm (–0.7). As can be seen, both systems demonstrate very similar ECD both in shape and energetic position and magnitude of particular bands, except for the region between about 375 and 400 nm where **Pt2** shows significantly increased intensity compared to **Pt1**. Finally, specific optical rotations (in deg cm^3 g^{-1} dm^{-1}) were measured in toluene for both complexes with values $[\alpha]_D^{23}$ = ±950 for **Pt1** and ±749 for **Pt2** (C = 1.0 mg mL^{-1}).

Considering that specific solvent effects and vibronic contributions have not been taken into account in the calculations, the simulated UV-vis and ECD spectra (computed using time-dependent DFT (TDDFT) with PBE0//SDD/SV(P) and the continuum solvent model for toluene)[17] agree satisfactorily with the experimental data (Fig. 2; see also the Computational details section and Fig. S2.2 in ESI†). In particular, energetic positions and signs of the bands are correctly reproduced by the theory along with an increased UV-vis intensity within the examined spectral range and enhanced ECD intensity of the low-energy tail of the spectra observed for **Pt2** *vs.* **Pt1**. The calculations also reproduce correctly the decrease in specific optical rotation values that accompanies the change from acac in **Pt1** to dbm in **Pt2** (with the better numerical agreement between experimental and theoretical results obtained for the BHLYP functional in line with the previously observed trends,[18] see Table S2.1 in ESI†).

Analysis of molecular orbital (MO) pair contributions to computed excitations shows that for both complexes, the main UV-vis and (positive) ECD intensity observed experimentally between about 300 and 375 nm originates from excitations predominantly corresponding to π–π* transitions within NHC-helicene ligand mixed with anisole → NHC-helicene intraligand charge transfer (ILCT), β-diketonato → NHC-helicene ligand–ligand CT (LLCT) and platinum(II) → NHC-helicene metal–ligand CT (MLCT), *vide infra*. See, for example, excitations no. 3 and 7 for **Pt1** and no. 5 and 11 for **Pt2**, calculated at respectively 349 and 316 nm (Fig. 2c and d, and ESI†), with the lower-energy excitation involving HOMO, HOMO−1, LUMO, LUMO+1 for **Pt1** and HOMO, HOMO−1, LUMO+1, LUMO+2 for **Pt2** (see Fig. 2e and ESI†). Note that the aforementioned **Pt2** rotameric structures considered in the computations demonstrate practically identical UV-vis spectra and very similar ECD envelopes that differ mostly only in the intensity of the higher-energy bands but without a change in the dominant electronic character of the underlying excitations (see ESI†). The lowest-energy excitations calculated for **Pt1** (no. 1 (389 nm) and 2 (365 nm)) also involve the aforementioned frontier MOs but they are mainly assigned to anisole-Pt → NHC-helicene ILCT and MLCT, and demonstrate rather modest oscillator (f) and rotatory strength (R) values. On the contrary, at wavelength longer than 350 nm, four excitations were computed for **Pt2**, all of enhanced f and/or R as compared to **Pt1** in line with increased UV-vis and ECD intensity observed in this spectral region for the dbm-based Pt complex. These excitations (no. 1 (394 nm), 2 (385 nm), 3 (365 nm), 4 (362 nm)) also involve the frontier MOs and collectively show strong anisole-Pt → NHC-helicene ILCT and MLCT character but with admixture of anisole-NHC-helicene-Pt → dbm LLCT and MLCT due to the presence of the extended π-electron system within the phenyl-substituted β-diketonate ligand resulting in the dbm-centred LUMO[13b] (see Fig. 2 and ESI†). In particular, the lowest-energy excitation no. 1 for **Pt2** corresponds to almost pure HOMO → LUMO anisole-NHC-Pt → dbm LLCT and MLCT and demonstrates negative rotatory strength. Finally, it should be highlighted that the aforementioned additional π-chromophoric dbm unit in **Pt2** clearly contributes to an increased UV-vis intensity observed for this complex compared to **Pt1** even at shorter wavelengths (around 300 nm); see for example excitation no. 13 computed at 308 nm (Fig. 2c and ESI†) and assigned to anisole-Pt-dbm → dbm π–π* transition mixed with ILCT, LLCT, and MLCT.

Both complexes are luminescent in deoxygenated toluene solution at room temperature. The emission spectrum recorded for **Pt1** (Fig. 3a; see also Table 1 for numerical data) displays some vibrational structure, with a (0,0) band at about 530 nm, whilst the (0,1) component at about 560 nm is the most intense; these wavelengths correspond to a vibrational progression of 1300 cm^{-1} associated with the C=C stretch of the aromatics, quite typical of many phosphorescent cyclometalated complexes.[19] The quantum yield under these conditions is 5%. The spectrum of **Pt2** covers a similar spectral region to that of **Pt1** but lacks any clear vibrational structure, despite a higher quantum yield of 9%. Much of the previous literature on NHC-Pt(II) complexes reports quantum yields only in films, rather than in solution,[7,13] so a direct comparison of the aforementioned quantum yield values for **Pt1** and **Pt2** with those obtained for related non-helicenic complexes is not readily possible. Compared to classical NHC-Pt systems, however, it appears that the helicene ligand imparts greater

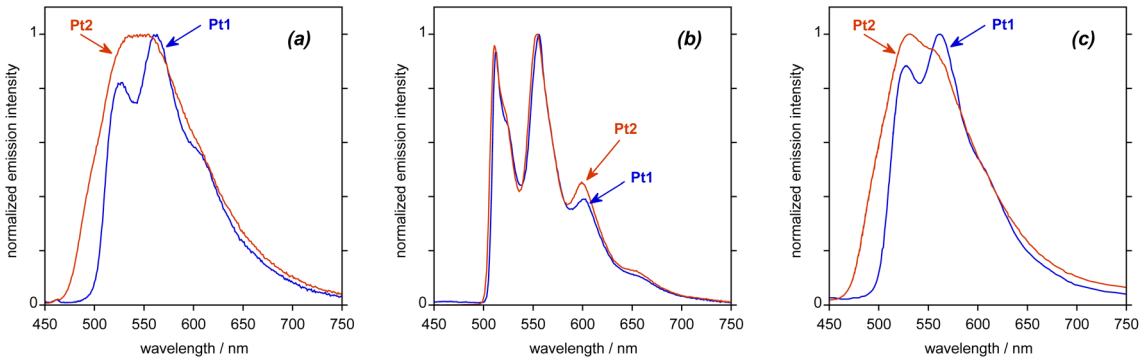

Fig. 3 Experimental emission spectra of **Pt1** and **Pt2** upon excitation at 400 nm: (a) in deoxygenated toluene solution at 295 K, (b) in butyronitrile at 77 K, and (c) in PMMA film (2 wt%) at 295 K under an atmosphere of nitrogen gas. See also Table 1 for numerical data.

Table 1 Photophysical properties of **Pt1** and **Pt2** complexes under the conditions indicated

Complex	Absorption in toluene at 295 K λ_{max}/nm (ε/10^3 M^{-1} cm^{-1})	Emission in toluene at 295 K [a]					Emission in PMMA film (2% w/w) at 295 K [b]					Emission in C_3H_7CN at 77 K	
		λ_{max}/nm	Φ_{lum}	τ/μs	k_r/s^{-1}	Σk_{nr}/s^{-1}	λ_{max}/nm	Φ_{lum}	τ/μs	k_r/s^{-1}	Σk_{nr}/s^{-1}	λ_{max}/nm	τ/μs
Pt1	306 (32.9), 338 (22.4), 383 (7.24), 402 (4.56), 441 (1.1)	526, 562, 605	0.05	290	170	3300	528, 562, 609	0.31	3200[c]	97	216	512, 556, 601, 657	3700
Pt2	308 (37.9), 336 (30.3), 385 (10.5), 403 (7.23), 441 (1.27)	546	0.09	65	1400	14 000	532, 555	0.23	1200[c]	192	642	511, 554, 599, 654	6400

[a] Values refer to degassed solutions; the quantum yields Φ_{lum} were measured relative to $[Ru(bpy)_3]Cl_2$ in aqueous solution for which Φ_{lum} = 0.04. [b] Data were recorded for thin films under an atmosphere of nitrogen gas; spectra and quantum yields were measured using an integrating sphere. [c] The decays in films do not fit to a single-exponential decay owing to heterogeneity in the environment of the molecules in the film: the quoted values are amplitude-weighted average lifetimes obtained from fitting to the sum of two exponential decays, as shown in Fig. S1.15 in ESI.†

rigidity to the complex that helps to reduce some of the deactivation pathways. Overall, the obtained quantum yields are in the same range as those reported for other helicene-NHC-transition-metal complexes.[11,12]

The luminescence decays mono-exponentially in both cases, with a lifetime of 290 μs for **Pt1** and 65 μs for **Pt2**. The fact that the lifetime is significantly shorter for **Pt2**, despite its higher quantum yield, suggests that the emission is "more allowed" (exhibits a higher participation of Pt orbitals) in **Pt2** than in **Pt1**. Further insight may be obtained by estimating the radiative k_r and non-radiative $\sum k_{nr}$ rate constants, assuming that the emitting state is formed with unit efficiency, through the relationships $k_r = \Phi/\tau$ and $\sum k_{nr} = (1 - \Phi)/\tau$. Such an analysis gives k_r values of 1400 and 170 s^{-1} for **Pt2** and **Pt1**, respectively. The order of magnitude difference suggests that the emissive excited state has significantly different orbital parentage in the two complexes. Conversely, the non-radiative decay is faster in **Pt2** than in **Pt1**, the estimated $\sum k_{nr}$ values being 14 000 and 3300 s^{-1}, respectively. Strassner and co-workers also observed a disappearance of a clear vibrational structure and substantial decrease in the lifetime of emission upon changing from acac to dbm in related Pt(II) complexes with a dibenzofuran NHC ligand, albeit in thin film rather than in fluid solution.[13] In that case, however, the changes were accompanied by a drop in the quantum yield and a significant red-shift in the emission (not observed in **Pt2**), features that were attributed to the phenyl rings of the dbm extending the π-electron system of this ligand,[13b] *vide infra*.

In a frozen glass in butyronitrile (C_3H_7CN) at 77 K, the vibronic structure becomes very well defined for both complexes, with $\lambda(0,0)$ = 514 nm in both cases (Fig. 3b and Table 1). Under these conditions, the lifetimes for **Pt1** and **Pt2** become very long (3.7 and 6.4 ms, respectively). This behaviour is consistent with a largely ligand-centred state localized on an extended π-electron system, as observed in some of our previous studies on complexes of other metals like Ir(III) and Re(I) with helicene ligands.[12a,c,e,20] Note that very similar vibronically structured phosphorescence signals were recorded in 2-methyltetrahydrofuran (2-MeTHF) at 77 K (see Fig. 4c).

The CPL spectra of (*P*) and (*M*) enantiomers of the **Pt1** and **Pt2** complexes were initially recorded in degassed toluene at room temperature (Fig. 4a and b). Pleasingly, well-structured CPL responses were obtained for both complexes, with dissymmetry factors $g_{lum} = 2(I_L - I_R)/(I_L + I_R)$ of +5 × 10^{-3} for (*M*)-**Pt1** and −3.9 × 10^{-3} for (*P*)-**Pt1** at 546 nm, and of +1.8 × 10^{-3} for (*M*)-**Pt2** and −1.9 × 10^{-3} for (*P*)-**Pt2** at 543 nm. Note that while the measured CPL spectra demonstrate overall similar shape, some bands have different signs for **Pt1** and **Pt2**. The CPL responses were then also recorded in a glass of 2-MeTHF at 77 K (Fig. 4c).[21] To our delight, the (*P*) and (*M*) enantiomers of both systems revealed mirror-image signals in the same region as the non-polarized fluorescence. In this case, the measured g_{lum} values were 1.3 × 10^{-2} for **Pt1** and 6.2 × 10^{-3} for **Pt2**, the former being one of the highest values reported up to now for Pt-helicene derivatives.[7a,11,16b] Unlike for the signals recorded in toluene at room temperature, the corresponding enantio-

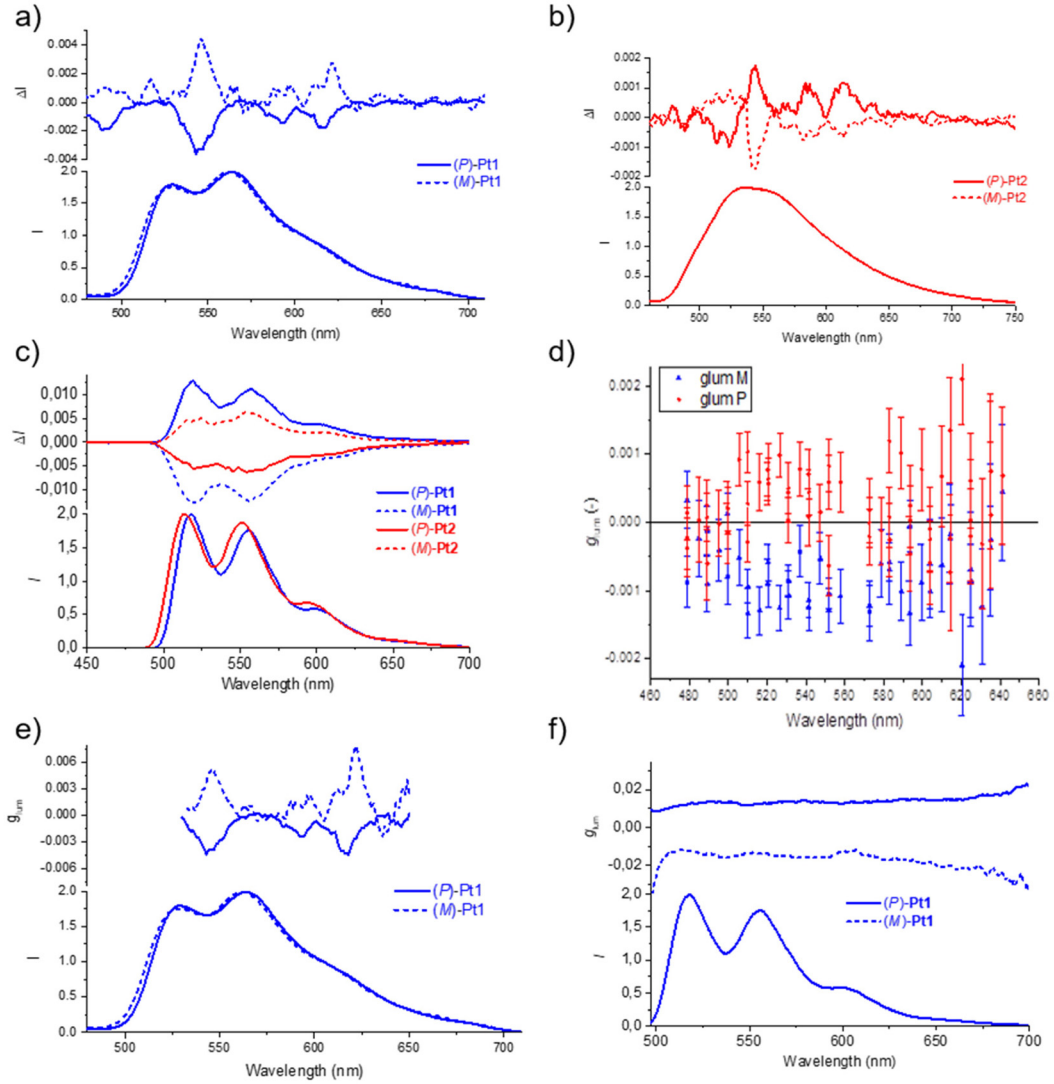

Fig. 4 Experimental luminescence and CPL spectra of (*P*) and (*M*) enantiomers of (a) **Pt1** and (b) **Pt2** in degassed toluene at room temperature (298 K), and of (c) **Pt1** and **Pt2** in degassed 2-MeTHF at low temperature (77 K); $C = 10^{-5}$ M, λ_{ex} = 365 nm. (d) Plot of g_{lum} values with emission wavelength obtained for 2 wt% PMMA film of **Pt1** enantiomers; λ_{ex} = 313 nm. (e) and (f) Comparison of g_{lum} values for **Pt1** enantiomers obtained at room temperature in toluene and at low temperature in 2-MeTHF, respectively.

mers of **Pt1** and **Pt2** display opposite CPL signs at 77 K (for (*P*) enantiomer: positive for **Pt1** *vs.* negative for **Pt2**). Note also that, interestingly, the more resolved CPL spectra at room temperature offer the advantage of observing the vibronic structure, contrary to the non-polarized luminescence (Fig. 4a and b).[16c] Meanwhile, at 77 K, both CPL and non-polarized phosphorescence become well-resolved and the vibronic structure appears clearly in Fig. 4c.

Fig. 4e and f display the g_{lum} values of **Pt1** enantiomers at room and low temperature, respectively, and the results are interesting to comment. Typically, if an optical transition derives from just two electronic states, ground and excited, then its g_{lum} value should be constant throughout the emission band. This is clearly not the case for the complexes examined here at room temperature, as visible in Fig. 4e for **Pt1**. There might be thus several electronic excited states involved in the signal under this condition. In addition, vibronic mixing may be involved in the excited states. Indeed, due to vibrational motion in the excited states, two different electronic states could get mixed. This very commonly leads to rapid variations in the g_{lum} value across the emission band.[21,22] The electronic states that get mixed into the lowest excited state each bring their own electric and magnetic transition dipole moments.

To shed some light on the electronic origin of the emissive properties for **Pt1** and **Pt2**, TDDFT calculations were then performed involving T_1 excited-state geometry optimizations. Representative results can be found in Fig. 5, which presents the electron density differences between the ground state and the excited state computed for both complexes, with their

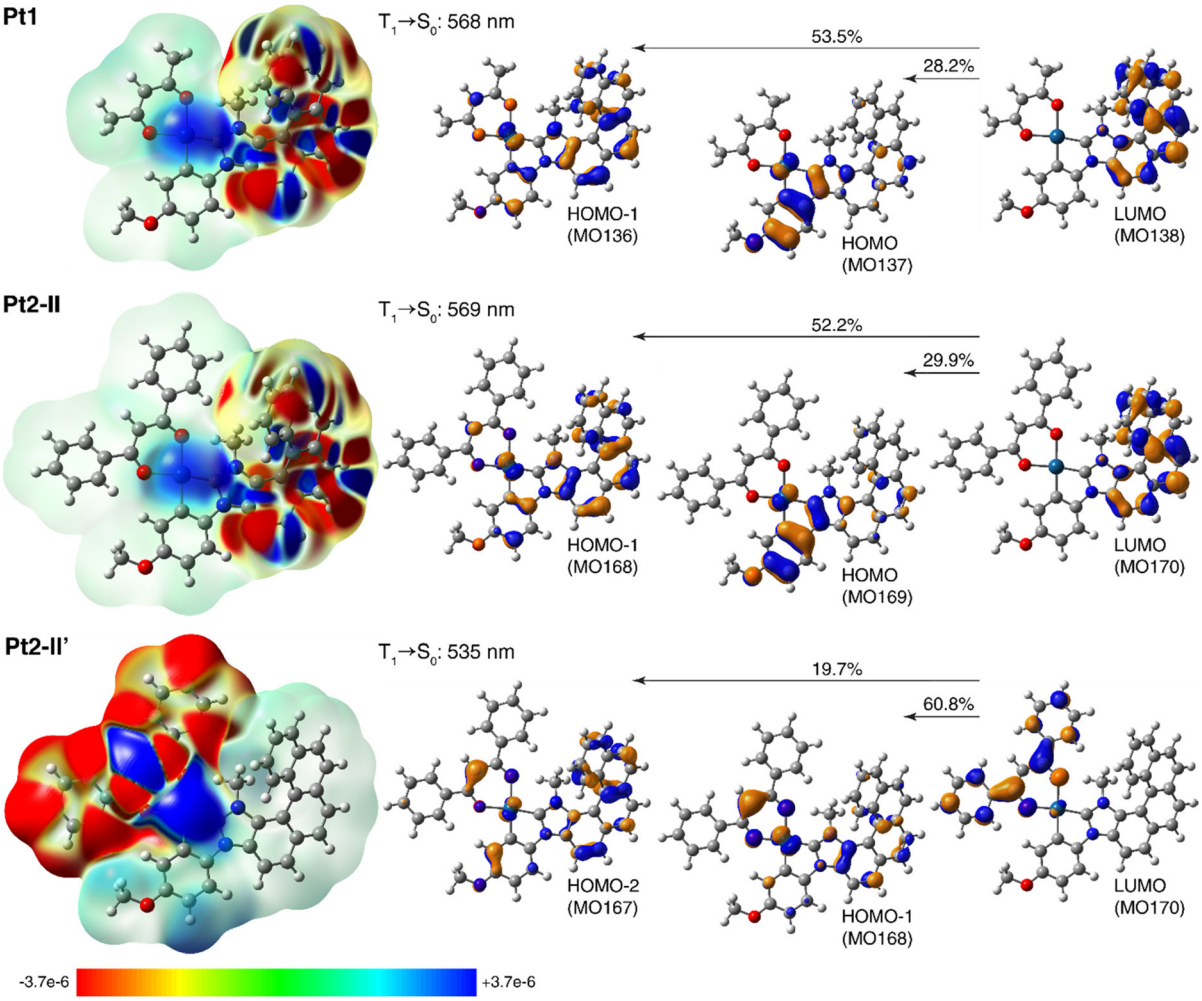

Fig. 5 Left: Electron density differences between the S_0 ground state and T_1 excited state, $\Delta\rho = \rho_g - \rho_e$, color-mapped on ρ_g (isosurfaces: ±0.0001 au) for **Pt1** and **Pt2** (in two conformations) based on the TDA-TDDFT-PBE0//SDD/SV(P) PCM(toluene) calculations. Electron density moves from the red region to the blue region when moving from the excited state to the ground state. Right: The corresponding computed $T_1 \rightarrow S_0$ phosphorescence wavelengths along with dominant MO-pair contributions (isosurfaces: ±0.04 au) to emission transition. See ESI† for a full set of calculated data.

negative (red)/positive (blue) values corresponding to outflow/inflow of electron density accompanying $T_1 \rightarrow S_0$ phosphorescence transition, along with the corresponding dominant MO-pair contributions. See Fig. S2.8–S2.12 and Tables S2.7, S2.8 in ESI† for additional calculated data.

As can be seen from Fig. 5 and data presented in the ESI,† the computations reproduce correctly the experimental energies of **Pt1** and **Pt2** emission, and in the case of **Pt2** seem to confirm that the existence of (structurally and/or electronically) different excited states may indeed be responsible for its experimentally observed emission features. Namely, for this system several T_1 excited-state structures were obtained including the expected (practically isoenergetic) rotamers (I–IV) of the phenyl groups in the dbm moiety corresponding to S_0 ground-state geometries, but also structures with the carbon C(Ph)C(H)C(Ph) chain of the dbm core deviated out the plane of the metalacycle OPtO and the two phenyl rings in the dbm ligand arranged more closely to planarity with this chain (II′ and II″ of slightly higher energy compared to I–IV); see Fig. S2.8 and Tables S2.7, S2.8.† The aforementioned rotameric T_1 structures of **Pt2**, as illustrated for the conformer II in Fig. 5 (see also ESI†), show essentially the same emission wavelength as that calculated for **Pt1** along with the same electronic origin that corresponds to predominantly NHC-helicene-centred $^3\pi\pi^*$ state with some NHC-helicene → anisole-Pt ^{3}MLCT and ^{3}ILCT character (see alternating inflow (blue) and outflow (red) of electron density within the π-system of NHC-helicene moiety along with accumulation of electron density around the metal centre accompanying $T_1 \rightarrow S_0$ transition visible in the electron difference densities for **Pt1** and **Pt2-II** shown in the left part of Fig. 5; compare also with Fig. S2.12†). Note that going to the T_1 equilibrium **Pt2** structures of this type, there is some reorganization among the frontier unoccupied MOs (LUMO and LUMO+1) as compared to their corresponding S_0 equilibrium

structures, with a significant energetic stabilization of the NHC-helicene-centred π*-orbital, which accordingly becomes LUMO and results in a change of the assignment for $T_1 \rightarrow S_0$ phosphorescence transition *vs.* $S_0 \rightarrow S_1$ absorption (*vide supra*). The structural modifications observed in the T_1 **Pt2-II′** and **Pt2-II″** geometries, on the other hand, seem to favour extended π-delocalization within the β-diketonate ligand leading to a decrease in its corresponding π*-orbital energy, such that in these structures the LUMO is localized on the (O^O) ligand, as observed in the ground-state structures of this system. Consequently, the corresponding $T_1 \rightarrow S_0$ transition in such conformers appears blue-shifted as compared to that in rotamers I–IV, and is assigned as predominantly dbm-centred (phenyl → core) ^{3}ILCT admixed with dbm → anisole-NHC-helicene-Pt ^{3}MLCT and ^{3}LLCT, as visible in Fig. 5 and ESI.† Note that similar assignment was proposed for the related dbm-NHC-dibenzofuran Pt(II) complex.[13b] Finally, it is worth noting that while solvation (toluene *vs.* THF used as a model for 2-MeTHF) effects simulated in the computations *via* polarizable continuum model do not appear to affect the calculated emission wavelength, they significantly change the relative percentage of MO-pair contributions to the emission transition (see ESI†), thus additionally influencing the electronic character of the emitting state depending on the solvent. All this indicates that, depending on measurement conditions such as temperature and environment/solvent, the emission signal observed for **Pt1** and **Pt2** may stem either from one or from several emitting states of similar or different orbital parentage. This conclusion accords well with the experimental findings. For example, the phosphorescence emission originated from **Pt2-II′**-type T_1 structure (with visibly enhanced metal orbitals' involvement as compared to **Pt1**, see Fig. 5) is consistent with the higher radiative rate constant observed for **Pt2** *vs.* **Pt1**, and (cautiously speculating) it may be a reason for a change in the sign of the CPL signal observed experimentally for both systems (for (*P*) enantiomer: positive for **Pt1** *vs.* negative for **Pt2**). The co-existence of several emitting states of slightly different emission wavelengths and electronic origins accounts also for a complicated picture of the CPL responses observed experimentally for both complexes at room temperature. Of importance, might be also the aforementioned mixing of different (higher-energy) electronic states into the emitting excited-state.[21,22] Further computational studies, including spin–orbit coupling effects and possibly higher-order correlated methods, are needed to provide a detailed rationalization of all the experimental results for **Pt1** and **Pt2**,[20c,21,23] which we plan to report for these and other related systems elsewhere in the future.

Due to the long-lived phosphorescence of these helicene-NHC-based platinum(II) complexes, and hence the potential for triplet–triplet quenching, the solid-state luminescence properties of compounds **Pt1** and **Pt2** were better studied in amorphous poly(methyl methacrylate) (PMMA) films at room temperature with 2 wt% emitter concentration under inert conditions. The recorded emission spectra are shown in Fig. 3c. As can be seen, the spectrum of **Pt1** is similar to the spectrum obtained in toluene solution, with three vibrational components resolved. The spectrum of **Pt2** shows a more resolved spectral profile than the largely featureless spectrum observed in solution, no doubt reflecting the more rigid environment in the polymer host. The quantum yields are elevated compared to those recorded in solution, rising to 31 and 23% for **Pt1** and **Pt2**, respectively, which can reasonably be attributed to a decrease in the non-radiative decay processes. The emission in the films under an inert atmosphere is very long-lived. Neither case shows the temporal decay following single exponential kinetics, no doubt reflecting heterogeneity in the environment of the complexes in the film. The decays fit well to two exponents (see Fig. S1.15†), from which amplitude-weighted average lifetimes of 3200 and 1200 μs are estimated for **Pt1** and **Pt2**, respectively. These values are of a similar order of magnitude to those at 77 K, confirming that the incorporation of the compounds into the film leads to an environment that is sufficiently rigid to greatly attenuate non-radiative decay processes. On the other hand, even in the films, the emission is very efficiently quenched by oxygen. The decay kinetics in air-equilibrated *vs.* inert atmosphere conditions are compared in Fig. S1.15,† and average lifetimes of around 80 μs are obtained for the films in air.

Finally, the CPL responses of both complexes were also examined in PMMA films at room temperature with 2 wt% emitter concentration. The compounds were excited at 313 nm, and the samples were measured using an in-line geometry for excitation and emission collection, while the excitation light was depolarized using a bundle of optical fibers. The (*P*) and (*M*) enantiomers of **Pt1** show signals of opposite sign, similar to those for CPL at low temperature (Fig. 4d), with λ_{max} at 520 nm and g_{lum} of the order of 10^{-3}. However, for **Pt2**, the g_{lum} values were so small that they could not be determined. Note that while for **Pt2** the CPL signs remain unchanged (+ for (*M*) and − for (*P*)), for **Pt1** they have been inverted when going from room to low temperature, but they are the same in PMMA as at low temperature, thus again highlighting the influence of the environment.

Conclusions

In summary, we have successfully synthesized two novel, chiral helicene-NHC-based platinum(II) complexes (**Pt1** and **Pt2**, bearing acac and dbm ligands, respectively), and studied in detail their photophysical and chiroptical properties. They exhibit long-lived phosphorescence with moderate quantum yields. Overall, the helicenic backbone in the N-heterocyclic carbene ligand allowed us to introduce chirality within the structure, generating strong chiroptical responses (intense electronic circular dichroism and circularly polarized phosphorescence). Complex **Pt1** was found to exhibit strong CPL response both in solution (g_{lum} of the order of 10^{-2} at low temperature and around 10^{-3} at room temperature) and in the solid state (g_{lum} of the order of 10^{-3} in thin films at room temperature). Theoretical analysis enabled the different beha-

viors of **Pt1** and **Pt2** to be accounted for in terms of structural and electronic origins. Compared to the platinum(II) complexes already reported in the literature, thanks to the presence of the helicenic moiety, we observed one of the strongest circularly polarized luminescence g_{lum} (0.013 at low temperature).[7a] In addition, the steric protection imparted by the helicene allowed to study, for the very first time, the photophysics of square-planar cyclometalated NHC-Pt complexes in solution. Finally, the CPL measurements in solution allowed us to clearly observe the vibronic structure. Our further efforts are directed towards developments of chiral supramolecular assemblies of helical systems displaying Pt–Pt interactions for amplifying the circularly polarized phosphorescence.[24]

Author contributions

Conceptualization, formal analysis, validation, resources, writing – review & editing: J. C., M. S.-H., S. C. J. M., J. A. G. W.; investigation: D. K. (synthesis, characterization, computations), N. d. R. (synthesis, characterization), M. C. (X-ray structure analysis), N. V. (chiral HPLC separations), S. C. J. M. (solid-state CPL), E. V. P. & J. A. G. W. (photophysics in solution and films), M. S.-H. (computations); methodology: D. K., M. S.-H.; writing – original draft: D. K., N. d. R., J. C.; visualization: D. K., M. S.-H., S. C. J. M., E. V. P.; supervision: J. C., J. A. G. W., M. S.-H.; funding acquisition: J. C., E. V. P.; project administration: J. C.

Conflicts of interest

There are no conflicts to declare.

Acknowledgements

We acknowledge the Ministère de l'Education Nationale, de la Recherche et de la Technologie, the Centre National de la Recherche Scientifique (CNRS), and the European Commission Research Executive Agency (grant agreement number: 859752—HEL4CHIROLED—H2020-MSCA-ITN-2019) for financial support. The computational part of the study was supported by PL-Grid Infrastructure and the ACC Cyfronet AGH in Krakow, Poland. E. V. P. and J. A. G. W. acknowledge the EPSRC grant ref: EP/S012788/1.

References

1 (*a*) D. Bourissou, O. Guerret, F. P. Gabbai and G. Bertrand, *Chem. Rev.*, 2000, **100**, 39–91; (*b*) *N-Heterocyclic Carbenes: From Laboratory Curiosities to Efficient Synthetic Tools*, ed. S. Díez-González, RSC, Cambridge, UK, 2011; (*c*) M. N. Hopkinson, C. Richter, M. Schedler and F. Glorius, *Nature*, 2014, **510**, 485–496.

2 Selected examples: (*a*) V. César, S. Bellemin-Laponnaz and L. H. Gade, *Chem. Soc. Rev.*, 2004, **33**, 619–636; (*b*) S. Díez-González, N. Marion and S. P. Nolan, *Chem. Rev.*, 2009, **109**, 3612–3676; (*c*) S. J. C. Cazin, *N-Heterocyclic Carbenes in Transition Metal Catalysis and Organocatalysis*, Springer, 2011; (*d*) F. Wang, L.-J. Liu, W. Wang, S. Li and M. Shi, *Coord. Chem. Rev.*, 2012, **256**, 804–853; (*e*) D. Zhao, L. Candish, D. Paul and F. Glorius, *ACS Catal.*, 2016, **6**, 5978–5988; (*f*) M. Karras, M. Dąbrowski, R. Pohl, J. Rybácek, J. Vacek, L. Bednárová, K. Grela, I. Starý, I. G. Stará and B. Schmidt, *Chem. – Eur. J.*, 2018, **24**, 10994–10998; (*g*) J. Thongpaen, R. Manguin and O. Baslé, *Angew. Chem., Int. Ed.*, 2020, **59**, 10242–10251; (*h*) A. M. Ruiz-Varilla, E. A. Baquero, B. Chaudret, E. de Jesus, C. Gonzalez-Arellano and J. C. Flores, *Catal. Sci. Technol.*, 2020, **10**, 2874–2881.

3 (*a*) C. A. Smith, M. R. Narouz, P. A. Lummis, I. Singh, A. Nazemi, C.-H. Li and C. M. Crudden, *Chem. Rev.*, 2019, **119**, 4986–5056; (*b*) R. Tarrieu, I. H. Delgado, F. Zinna, V. Dorcet, S. Colombel-Rouen, C. Crevisy, O. Basle, J. Bosson and J. Lacour, *Chem. Commun.*, 2021, **57**, 3793–3796; (*c*) S. Dery, P. Bellotti, T. Ben-Tzvi, M. Freitag, T. Shahar, A. Cossaro, A. Verdini, L. Floreano, F. Glorius and E. Gross, *Langmuir*, 2021, **37**, 10029–10035.

4 *Highly Efficient OLEDs with Phosphorescent Materials*, ed. H. Yersin, Wiley VCH, 2008.

5 Selected examples of phosphorescent chiral Pt complexes in OLEDs: (*a*) J. R. Brandt, X. Wang, Y. Yang, A. J. Campbell and M. J. Fuchter, *J. Am. Chem. Soc.*, 2016, **138**, 9743–9746; (*b*) Z.-P. Yan, X.-F. Luo, W.-Q. Liu, Z.-G. Wu, X. Liang, K. Liao, Y. Wang, Y.-X. Zheng, L. Zhou, J.-L. Zuo, Y. Pan and H. Zhang, *Chem. – Eur. J.*, 2019, **25**, 5672–5676.

6 Selected examples of cycloiridiated NHC complexes in OLEDs: (*a*) T. Sajoto, P. I. Djurovich, A. Tamayo, M. Yousufuddin, R. Bau, M. E. Thompson, R. J. Holmes and S. R. Forrest, *Inorg. Chem.*, 2005, **44**, 7992–8003; (*b*) C.-F. Chang, Y.-M. Cheng, Y. Chi, Y.-C. Chiu, C.-C. Lin, G.-H. Lee, P.-T. Chou, C.-C. Chen, C.-H. Chang and C.-C. Wu, *Angew. Chem., Int. Ed.*, 2008, **47**, 4542–4545; (*c*) T.-Y. Li, X. Liang, L. Zhou, C. Wu, S. Zhang, X. Liu, G.-Z. Lu, L.-S. Xue, Y.-X. Zheng and J.-L. Zu, *Inorg. Chem.*, 2015, **54**, 161–173; (*d*) J. Lee, H.-F. Chen, T. Batagoda, C. Coburn, P. I. Djurovich, M. E. Thompson and S. R. Forrest, *Nat. Mater.*, 2016, **15**, 92–98; (*e*) P.-H. Lanoë, J. Chan, G. Gontard, F. Monti, N. Armaroli, A. Barbieri and H. Amouri, *Eur. J. Inorg. Chem.*, 2016, 1631–1634; (*f*) M. Zhang, S.-W. Zhang, C. Wu, W. Li, Y. Wu, C. Yang, Z. Meng, W. Xu, M.-C. Tang, R. Xie, H. Meng and G. Wei, *ACS Appl. Mater. Interfaces*, 2022, **14**, 1546–1556.

7 Selected examples of cycloplatinated NHC complexes in OLEDs: (*a*) X. Wang, S. Ma, B. Zhao and J. Deng, *Adv. Funct. Mater.*, 2023, 2214364; (*b*) T. Strassner, *Acc. Chem. Res.*, 2016, **49**, 2680–2689; (*c*) G. Li, S. Liu, Y. Sun, W. Lou, Y.-F. Yang and Y. She, *J. Mater. Chem. C*, 2022, **10**, 210–218; (*d*) R. He, R. A. Domingues, S. Valandro and K. S. Schanze, *Macromolecules*, 2021, **54**, 9888–9895; (*e*) V. Sicilia,

S. Fuertes, A. J. Chueca, L. Arnal, A. Martín, M. Perálvarez, C. Botta and U. Giovanella, *J. Mater. Chem. C*, 2019, **7**, 4509–4516; (*f*) X.-C. Hang, T. Fleetham, E. Turner, J. Brooks and J. Li, *Angew. Chem., Int. Ed.*, 2013, **52**, 6753–6756; (*g*) T. Fleetham, G. Li and J. Li, *Adv. Mater.*, 2017, **29**, 1601861.

8 (*a*) M. Lindemann, G. Xu, T. Pusch, R. Michalzik, M. R. Hofmann, I. Žutić and N. C. Gerhardt, *Nature*, 2019, **568**, 212–215; (*b*) H. Wang, L. Liu and C. Lu, *Procedia Comput. Sci.*, 2018, **131**, 511–519; (*c*) J. Han, S. Guo, H. Lu, S. Liu, Q. Zhao and W. Huang, *Adv. Opt. Mater.*, 2018, **6**, 1800538; (*d*) T. Novikova, A. Pierangelo, S. Manhas, A. Benali, P. Validire, B. Gayet and A. D. Martino, *Appl. Phys. Lett.*, 2013, **102**, 241103; (*e*) B. Kunnen, C. Macdonald, A. Doronin, S. Jacques, M. Eccles and I. Meglinski, *J. Biophotonics*, 2015, **8**, 317–323; (*f*) R. Carr, N. H. Evans and D. Parker, *Chem. Soc. Rev.*, 2012, **41**, 7673–7686; (*g*) T. Mori, *Circularly Polarized Luminescence of Isolated Small Organic Molecules*, Springer, Singapore, 2020.

9 D.-W. Zhang, M. Li and C.-F. Chen, *Chem. Soc. Rev.*, 2020, **49**, 1331–1343.

10 Chiral platinum complex bearing chiral monodentate NHCs: (*a*) D. Brissy, M. Skander, P. Retailleau and A. Marinetti, *Organometallics*, 2007, **26**, 5782–5785; (*b*) A. Meyer, M. A. Taige and T. Strassner, *J. Organomet. Chem.*, 2009, **694**, 1861–1868; (*c*) S. K. U. Riederer, B. Bechlars, W. A. Herrmann and F. E. Kühn, *Eur. J. Inorg. Chem.*, 2011, 249–254; (*d*) P. Marshall, R. L. Jenkins, W. Clegg, R. W. Harrington, S. K. Callear, S. J. Coles, I. A. Fallis and A. Dervisi, *Dalton Trans.*, 2012, **41**, 12839–12846.

11 (*a*) N. Saleh, C. Shen and J. Crassous, *Chem. Sci.*, 2014, **5**, 3680–3694; (*b*) H. Isla and J. Crassous, *C. R. Chim.*, 2016, **19**, 39–49; (*c*) J.-K. Ou-Yang and J. Crassous, *Coord. Chem. Rev.*, 2018, **376**, 533–547; (*d*) K. Dhbaibi, L. Favereau and J. Crassous, *Chem. Rev.*, 2019, **119**, 8846–8953; (*e*) E. S. Gauthier, R. Rodríguez and J. Crassous, *Angew. Chem., Int. Ed.*, 2020, **59**, 22840–22856.

12 (*a*) N. Hellou, M. Srebro-Hooper, L. Favereau, F. Zinna, E. Caytan, L. Toupet, V. Dorcet, M. Jean, N. Vanthuyne, J. A. G. Williams, L. Di Bari, J. Autschbach and J. Crassous, *Angew. Chem., Int. Ed.*, 2017, **56**, 8236–8239; (*b*) A. Macé, N. Hellou, J. Hammoud, C. Martin, E. S. Gauthier, L. Favereau, T. Roisnel, E. Caytan, G. Nasser, N. Vanthuyne, J. A. G. Williams, F. Berrée, B. Carboni and J. Crassous, *Helv. Chim. Acta*, 2019, **102**, e1900044; (*c*) E. S. Gauthier, L. Abella, N. Hellou, B. Darquié, E. Caytan, T. Roisnel, N. Vanthuyne, L. Favereau, M. Srebro-Hooper, J. A. G. Williams, J. Autschbach and J. Crassous, *Angew. Chem., Int. Ed.*, 2020, **59**, 8394–8400; (*d*) E. S. Gauthier, M. Cordier, V. Dorcet, N. Vanthuyne, L. Favereau, J. A. G. Williams and J. Crassous, *Eur. J. Org. Chem.*, 2021, 4769–4776; (*e*) E. S. Gauthier, N. Hellou, E. Caytan, S. Del Fré, V. Dorcet, N. Vanthuyne, L. Favereau, M. Srebro-Hooper, J. A. G. Williams and J. Crassous, *Inorg. Chem. Front.*, 2021, **8**, 3916–3925.

13 (*a*) A. Tronnier, A. Poethig, S. Metz, G. Wagenblast, I. Muenster and T. Strassner, *Inorg. Chem.*, 2014, **53**, 6346–6356; (*b*) A. Tronnier, U. Heinemeyer, S. Metz, G. Wagenblast, I. Muenster and T. Strassner, *J. Mater. Chem. C*, 2015, **3**, 1680–1693.

14 H. Zhang, Q. Cai and D. Ma, *J. Org. Chem.*, 2005, **70**, 5164–5173.

15 (*a*) Y. Unger, D. Meyer, O. Molt, C. Schildknecht, I. Munster, G. Wagenblast and T. Strassner, *Angew. Chem., Int. Ed.*, 2010, **49**, 10214–10216; (*b*) G. L. Petretto, M. Wang, A. Zucca and J. P. Rourke, *Dalton Trans.*, 2010, **39**, 7822–7825; (*c*) S. Fuertes, A. J. Chueca and V. Sicilia, *Inorg. Chem.*, 2015, **54**, 9885–9895.

16 (*a*) L. Norel, M. Rudolph, N. Vanthuyne, J. A. G. Williams, C. Lescop, C. Roussel, J. Autschbach, J. Crassous and R. Réau, *Angew. Chem., Int. Ed.*, 2010, **49**, 99–102; (*b*) J. Crassous, I. G. Stará and I. Starý, *Helicenes: Synthesis, Properties and Applications*, John Wiley & Sons, Ltd, 2022; (*c*) D. Schnable, N. D. Schley and G. Ung, *J. Am. Chem. Soc.*, 2022, **144**, 10718–10722.

17 (*a*) M. Srebro-Hooper, J. Crassous and J. Autschbach, in *Helicenes: Synthesis, Properties and Applications*, ed. J. Crassous, I. G. Stará and I. Starý, John Wiley & Sons, Ltd, 2022, vol. 12, pp. 395–421; (*b*) M. Srebro-Hooper and J. Autschbach, *Annu. Rev. Phys. Chem.*, 2017, **68**, 399–420; (*c*) J. Autschbach, *Chirality*, 2009, **21**, E116–E152.

18 M. Srebro, N. Govind, W. A. de Jong and J. Autschbach, *J. Phys. Chem. A*, 2011, **115**, 10930–10949.

19 A. F. Rausch, L. Murphy, J. A. G. Williams and H. Yersin, *Inorg. Chem.*, 2009, **48**, 11407–11414.

20 (*a*) N. Saleh, M. Srebro, T. Reynaldo, N. Vanthuyne, L. Toupet, V. Y. Chang, G. Muller, J. A. G. Williams, C. Roussel, J. Autschbach and J. Crassous, *Chem. Commun.*, 2015, **51**, 3754–3757; (*b*) N. Saleh, D. Kundu, N. Vanthuyne, J. Olesiak-Banska, A. Pniakowska, K. Matczyszyn, V. Y. Chang, G. Muller, J. A. G. Williams, M. Srebro-Hooper, J. Autschbach and J. Crassous, *ChemPlusChem*, 2020, **85**, 2446–2454; (*c*) H. D. Ludowieg, M. Srebro-Hooper, J. Crassous and J. Autschbach, *ChemistryOpen*, 2022, **11**, e202200020.

21 K. Dhbaibi, P. Morgante, N. Vanthuyne, J. Autschbach, L. Favereau and J. Crassous, *J. Phys. Chem. Lett.*, 2023, **14**, 1073–1081.

22 H. P. J. M. Dekkers and L. E. Closs, *J. Am. Chem. Soc.*, 1976, **98**, 2210–2219.

23 F. Gendron, B. Moore II, O. Cador, F. Pointillart, J. Autschbach and B. Le Guennic, *J. Chem. Theory Comput.*, 2019, **15**, 4140–4155.

24 G. Park, H. Kim, H. Yang, K. R. Park, I. Song, J. H. Oh, C. Kim and Y. You, *Chem. Sci.*, 2019, **10**, 1294–1301.